

Accepted by AJ

Mid-infrared Identification of 6 cm Radio Source Counterparts in the Extended Groth Strip

S. P. Willner,¹ A. L. Coil,^{2,3} W. M. Goss,⁴ M. L. N. Ashby,¹ P. Barmby,¹
J.-S. Huang,¹ R. Ivison,^{5,6} D. C. Koo,⁷ E. Egami⁸ & Satoshi Miyazaki⁹

ABSTRACT

A new 6 cm survey of almost 0.6 deg^2 to a limit of 0.55 mJy/beam (10σ) finds 37 isolated radio sources and 7 radio source pairs (not necessarily physical companions). IRAC counterparts are identified for at least 92% of the radio sources within the area of deep IRAC coverage, which includes 31 isolated sources and 6 pairs. This contrasts with an identification rate of $<74\%$ to $R < 23.95$ in visible light. Eight of the IRAC galaxies have power law spectral energy distributions, implying that the mid-infrared emission comes from a powerful AGN. The remaining 26 IRAC galaxies show stellar emission in the mid-infrared, probably in most of these galaxies because the stellar emission is bright enough to outshine an underlying AGN. The infrared colors suggest that the majority of these galaxies are bulge-dominated and have redshifts $0.5 \lesssim z \lesssim 1$. Visible

¹Harvard-Smithsonian Center for Astrophysics, 60 Garden Street, Cambridge, MA 02138

²Department of Astronomy, University of California, Berkeley, CA 94720-3411

³Hubble Fellow, Steward Observatory, University of Arizona, Tucson, AZ 85721

⁴National Radio Astronomy Observatory, P.O. Box 0, 1003 Lopezville Road, Socorro, NM 87801

⁵Astronomy Technology Centre, Royal Observatory, Blackford Hill, Edinburgh EH9 3HJ UK

⁶Institute for Astronomy, University of Edinburgh, Blackford Hill, Edinburgh EH9 3HJ UK

⁷UCO/Lick Observatory, Dept. of Astronomy & Astrophysics, Univ. of California, Santa Cruz, CA 95064

⁸Steward Observatory, University of Arizona, 933 North Cherry Avenue, Tuscon, AZ 85721

⁹Subaru Telescope, National Astronomical Observatory of Japan, 650 North A'ohoku Place, Hilo, HI 96720

spectra from the DEEP2 redshift survey, available for 11 galaxies, are consistent with this suggestion. The IRAC galaxies fall into two distinct groups in a color-magnitude diagram, one group (the “stripe”) includes all the AGN. The other group (the “blue clump”) has blue 3.6 to 8 μm colors and a small range of 8 μm magnitudes. This separation should be useful in classifying galaxies found in other radio surveys.

Subject headings: keywords

1. Introduction

Radio observations are an excellent way to identify star-forming galaxies and active galactic nuclei (AGN), being subject to fewer selection effects than optical surveys (e.g. obscuration; spectral line contamination). Until recently a large fraction of the most distant known galaxies had first been detected in radio surveys, their nature betrayed by steep radio spectra and faint optical/infrared (opt/IR) counterparts (e.g., van Breugel et al. 1999). Indeed, the discovery by Minkowski (1960) that 3C 295 — an object we shall meet later in this paper — lies at $z = 0.461$ (at that time the most distant known object) was due to its initial detection at 159 MHz and a photometric redshift prediction by Baum (1957) of the kind that is now commonplace (e.g., Blake & Bridle 2005).

Wide, low-frequency surveys such as 3CR tend to yield associations with bright ellipticals (radio galaxies) and a smattering of radio quasars and BL Lacs (e.g., Spinrad, Marr, Aguilar, & Djorgovski 1985), whereas at higher frequencies (e.g. 5 GHz) radio quasars become more common. At lower flux densities, around 1 mJy, the source counts steepen: evidence of either primeval radio galaxies (Windhorst 1986) or that the star-forming galaxies play an increasingly important role (van der Laan, Katgert, Windhorst, & Oort 1983). Indeed, for low radio luminosities ($L_{1.4\text{GHz}} \leq 10^{23} \text{ W Hz}^{-1}$) Yun, Hibbard, Condon, & Reddy (1999) argue that the fraction of AGN in radio-selected samples drops to around 10%, as revealed via an excess of radio emission above that predicted by the far-IR/radio correlation (e.g., Helou, Soifer, & Rowan-Robinson 1985). All of these AGN also reveal their nuclear activity in the mid-infrared or X-ray wavebands.

Determining the nature of faint radio sources is non-trivial. Even the first step — obtaining optical or IR identifications — can be time consuming, a task that

ultimately yields little but a slit position for spectroscopic follow up and a very basic measure of stellar mass and star-formation rate, both subject to obscuration by dust for galaxies at high redshift.

This paper presents moderately-deep radio observations of the Extended Groth Strip (EGS) obtained at a wavelength of 6 cm using the Very Large Array. Deeper observations at 20 cm have been obtained (Ivison et al. 2006), but this paper gives an overview of the counterparts of the bright population, those sources we expect to be dominated by AGN. For distant galaxies, the rest-frame near-IR observations provided by *Spitzer* enable relatively easy identifications and the best possible measure of stellar mass (e.g., Bell & de Jong 2001) and hence of the likely evolutionary state of a radio galaxy.

Throughout this paper, magnitudes are in the Vega system, and the notation $[w]$ means the Vega magnitude at wavelength w .

2. VLA Observations

The EGS is a region of sky that includes the original HST WFPC2 Groth Strip Survey. (See Vogt et al. 2005 for details of the original HST survey.) The EGS is centered near J2000 RA= $14^h 19^m 00^s$ Dec= $52^\circ 50' 00''$ and covers roughly 2° by 0.25° at a position angle of 50° . Observations within the EGS (many now being labelled “AEGIS”) include deep optical imaging, deep *Spitzer* mid-IR imaging (Fazio et al. 2004b; Barmby et al. 2006), and X-ray observations with both Chandra (Nandra et al. 2005) and XMM Newton (Waskett et al. 2003). There is also Keck spectroscopy from the DEEP2 Redshift Survey (Davis et al. 2003) covering the redshift range $0.1 < z < 1.4$ for normal galaxy types. Not all observations cover the entire strip area. In particular, the *Spitzer* observations include only a $10'$ -wide strip centered within the EGS region. Davis et al. (2006) summarize many of the data sets.

We chose to image the EGS with the VLA at 6 cm instead of 20 cm because the bright radio source 3C 295 is located nearby at RA= $14^h 09^m 33.49^s$ and Dec= $52^\circ 26' 13.0''$ (J2000), only $8.5'$ from the southwest corner of the *Spitzer* coverage in the EGS. At 6 cm, contamination levels are much lower than at 20 cm because 3C 295 is a factor of 3.5 times fainter and 3.3 times farther away in terms of the primary beam size. The shorter observing wavelength makes this survey relatively more sensitive to flat-spectrum radio sources than a 20 cm survey would be.

The observations were obtained at the Very Large Array (VLA) in BnA configuration for a total of 19 hours over 3 days from 2003 October 11–13 (program AW615). This configuration gives wide coverage on the sky with angular resolution similar to that of the IRAC imaging data, as required for identifying IRAC counterparts to the radio sources. At 4.8 GHz the VLA antennas have a primary beam with a FWHM of 9'. The mapping grid contained 74 pointings, spaced 5' apart, providing roughly uniform sensitivity beyond the full Spitzer area in the EGS. Each pointing center was observed for 15 minutes. The observations were carried out in continuum mode with two intermediate frequency (IF) bands, each 50 MHz wide, centered at 4885 and 4835 MHz. The point source VCS2 J1400+6210 (=4C 62.22) was observed for 2 minutes every 17 minutes to provide phase calibrations. Phase stability was sufficient to give astrometric accuracy better than 0''.1 rms. We observed the flux calibrators 3C 286 for 12 minutes on October 12 and 3C 48 for 15 minutes on October 13. No flux calibrator was observed on October 11.

The data were reduced using the AIPS software package. We used TVFLG to ignore bad visibility data with discrepant amplitude values. Flux calibrations were derived from observations of 3C 286 and 3C 48, which gave 1.71 Jy for the flux density of the phase calibrator. Measurements with the two primary calibrators agreed within 2%, which we take as an estimate of the flux calibration uncertainty. We then used 4C 62.22 to provide phase calibrations and amplitudes for the October 11 data. Images containing bright (>10 mJy/beam) point sources were self-calibrated.

For each of the 74 pointings we used the IMAGR task in AIPS to create a 2048x2048 pixel image with a pixel scale of 0''.4 per pixel. ROBUST was set to 0, which is an intermediate case between uniform and natural weighting of the sparsely-sampled UV points, and UVTAPER was set to 170 $k\lambda$, effectively de-weighting the A-array elements and reducing the elongation of the synthesized beam. To avoid clean bias we CLEANed the images to a flux level of 260 μ Jy/beam, corresponding to $\sim 4\sigma$ rms, which typically took 100–200 CLEAN iterations. The 1σ rms in these images is ~ 60 –70 μ Jy/beam. Each image is 13''.65 on a side, larger than the FWHM of the primary beam. The synthesized beam is approximately 1''.0 by 1''.5 at a PA of 25°, but it varies slightly from pointing to pointing. This size is similar to the IRAC FWHM of 1''.7–2''.0 (Fazio et al. 2004a). We also imaged a small region at the location of 3C 295 and found no residual flux with an rms noise of 67 μ Jy/beam. Thus any artifacts from 3C 295 should be below the 1σ level.

For each quarter of the length of the strip, overlapping images were combined

into a mosaic using the LINMOS routine in the MIRIAD software package. This routine does a simple linear mosaicing. In the four mosaic images, within the FWHM of the overlapping primary beams, the rms noise is $42 \mu\text{Jy}/\text{beam}$. Initial source detection was performed on these mosaic images using SExtractor with a threshold of $143 \mu\text{Jy}/\text{beam}$. Each potential source was then checked in the original images (not mosaics), and sources below 10σ were removed from the list. This conservative detection limit was needed to avoid spurious sources; many 5σ bumps are real, but many are sidelobes caused by the limited UV coverage. Many radio surveys with better sensitivity are available, including in the EGS (Ivison et al. 2006), and the purpose of this paper is best served by maximizing reliability. We used the AIPS task JMFIT to determine final sources positions and flux densities and corrected the latter for delay beam distortions (Condon et al. 1998).

3. Radio Source Counterparts

Altogether 51 radio components (some of which may be radio doubles) were detected in an area of 0.5735 deg^2 (the 50% primary beam limit). This agrees well with the number of sources expected on the basis of previous surveys (45, based on an average sensitivity limit of $0.55 \text{ mJy}/\text{beam}$ — Ciliegi et al. 2003). Table 1 lists the source catalog and parameters of each source: name,¹ position, primary beam correction, corrected total flux density, and deconvolved angular size if the source is resolved. For source pairs, components are listed separately regardless of the likelihood of physical association. Table 1 includes 37 isolated sources and seven pairs with separations in the range $3''$ to $13''$. For three cases (10/11, 17/18, and 50/51), the radio morphology is that of a classical double. For the other five cases, we cannot tell from the radio morphology alone whether they are classical doubles or separate sources. For the closest pairs, where the two components might be blended at the VLA resolution, combined flux densities are given as well as separate ones for each component.

Fomalont et al. (1991, hereafter FWKK) surveyed a small part of the present EGS field to much deeper flux density, a completeness limit of $25 \mu\text{Jy}$ at 5 GHz. They found 8 sources within our coverage area and with flux densities greater than 0.2 mJy .

¹Radio sources from this paper are named EGS06 followed by the cardinal number given in Table 1. The ‘06’ in the name refers to the observation wavelength in centimeters.

Table 2 compares our results with those of FWKK. Our survey detected the four sources with the highest flux densities but not the four faintest, as expected. For the seven pointlike sources, flux densities or upper limits agree within the uncertainties except perhaps for EGS06 23=15V70, which might have varied in the 14+ years between surveys. Source 21=15V10 is extended, and it is hard to make a direct comparison between the two surveys because they used different VLA configurations. All in all, the two surveys agree within their limited area of overlap.

The position of each radio source was examined in the IRAC 3.6 to 8 μm images of the EGS. These images have angular resolution (FWHM) of 2" and 5 σ sensitivities 0.9 to 6.2 μJy (Barmby et al. 2006; Davis et al. 2006). Eight radio sources or pairs are outside the IRAC coverage area.² Of 31 isolated radio sources inside the IRAC coverage area (first part of Table 1), 28 have IRAC counterparts within 0".8, and the other three have no IRAC counterpart closer than 1".2. We consider the first group identified and the second group not. Trials with random positions suggest about 1.5% chance of an IRAC source within 0".8 of a given position; i.e., zero to one of the IRAC counterparts may be spurious on this basis. However, most of the proposed counterparts have flux densities well above the IRAC survey limit, and spurious matches involving such bright sources are far less likely. Of five possible source pairs with IRAC coverage (second part of Table 1), the two pairs with radio morphology of classical doubles both have an IRAC source between the two radio components, as expected.³ Thus for 33 “easy” cases, we find IRAC counterparts for 30, an identification rate of 91%.

²Some of the sources “outside the IRAC area” have a few IRAC frames covering the position, but data are noisy and affected by cosmic rays. Sources 5/6 show an IRAC source at the position of the northern radio component (6) but nothing close to the southern one (5) (which may be slightly extended or double in the radio). This could be a double radio source with very different lobe distances from the host galaxy, or the radio sources could be unrelated with only the northern one having an IRAC counterpart, or the southern radio source, which has low signal-to-noise, might not be real. Most likely is that the IRAC observations are not deep enough to detect the true counterpart; despite that, we show the data for the source near EGS06 6 in tables and figures. Sources 17/18 have a faint IRAC source at 3.6 and 4.5 μm (2.7 and 3.7 μJy respectively) 0".9 north of the northern source (18), but we do not consider this a detection of a counterpart. Because the radio morphology is that of a classical double, we would expect the counterpart to be between the radio lobes. Source 32 and 48 have IRAC sources nearby but too far from the radio positions to be deemed counterparts. Deeper IRAC data would be needed to say more about these sources.

³IRAC exposure time for 50/51 is only 1/10 normal, but the source has high flux density and was reliably detected. However cosmic rays badly affect the 5.8 μm photometry.

The three additional radio source pairs are more difficult to assess. Source 26 is pointlike, but the nearby northern radio source (#27) shows multiple sub-components. An IRAC source is 4''.1 northeast of the southern radio source. (See Figure 1.) We consider this a valid counterpart to a likely radio double, despite the IRAC galaxy not being centered between the two radio sources. Radio sources 39/40 have wide separation, and there are additional, faint IRAC sources in the field. Any interpretation is uncertain, but we deem the brightest IRAC source, located between the two radio sources, a valid counterpart to a radio double. There is an IRAC source between sources 42/43, 2''.6 from #43. On higher resolution red images from Subaru, this source is double with separation 1''.4. We consider this a likely counterpart to the 42/43 pair. Thus our best guess is that we have three IRAC counterparts to three radio doubles and an overall identification rate of 33/36 = 92%. While these three identifications are uncertain, they won't change subsequent conclusions of this paper. IRAC positions are listed in Table 3.

The high identification rate (>90%) in the infrared contrasts with a much lower rate that would be found in visible light. Only 24 radio sources have R counterparts in the DEEP2 catalog ($R < 23.95$, Davis et al. 2003; see also Coil et al. 2004 and <http://deep.berkeley.edu/>), and of these, only 12 are brighter than $R = 21.5$. The faintness of the counterparts to 5 GHz radio sources found here contrasts with the results of a 1.4 GHz survey (Mobasher et al. 1999), where half the radio sources were found to have visible counterparts with $R < 21.5$. A more direct but smaller comparison sample is a 5 GHz survey in the Lockman Hole (Ciliegi et al. 2003). In that survey, of 12 radio sources with $S_{5\text{ GHz}} > 0.2$ mJy, 8 have counterparts with $I < 21$, although Ciliegi et al. accepted larger position offsets than we do. In contrast, we find counterparts that bright in I for only 14 of the EGS radio sources (with $S_{5\text{ GHz}} > 0.4$ mJy). Considering that the radio surveys have different depths, different wavelengths, different counterpart identification criteria, and are done in different regions of sky, there are probably no major inconsistencies in the fraction of counterparts optically identified.

Photometry of each IRAC counterpart was done on the four IRAC images and the MIPS 24 μm image.⁴ (The MIPS images are also described by Barmby et al. 2006.) A center position was measured on whichever image offered the best signal to noise ratio (usually 3.6 μm but sometimes longer wavelengths), and the IRAF task APPHOT was used to measure flux in a 5''.2 diameter beam. Sky was measured in an

⁴Sensitivity at 70 and 160 μm was not sufficient to say anything useful about individual sources.

annulus of radius between $17''$ and $24''$, though the exact choice did not matter. The IRAC sources are all pointlike, and flux densities are given in Table 4 based on the point source calibration. Except for sources near the edge of coverage (indicated in Table 4), all the detected counterparts are bright relative to the limiting magnitude of the images, and statistical uncertainties (given in the last row of Table 4) are small. Systematic uncertainties, due for example to centering errors or companion sources, are typically $\ll 5\%$ but can reach 10% for objects with nearby companions. Calibration uncertainty is about 3% (Reach et al. 2005).

Within the well-observed IRAC region, there are only three radio sources that may not have IRAC counterparts. Fig. 2 shows thumbnails of these. Sources 9 and 15 show faint radio extensions to the northeast and north, respectively. In each case, there is an IRAC and MIPS source within the radio extension $1''8$ and $4''1$ respectively from the radio peak positions.⁵ While these sources could be the radio counterparts, establishing them as such would require more evidence. Source 38 shows a bright galaxy ($167 \mu\text{Jy}$ at $3.6 \mu\text{m}$) located $2''.6$ southeast of the radio position.⁶ The high-resolution r image shows a much fainter galaxy ($r > 24$) $1''.4$ northwest of the bright one, $1''.2$ east of the radio source peak and within an eastward radio extension. This faint galaxy could be the counterpart, but at the low angular resolution of the infrared images it is difficult to distinguish from the bright galaxy nearby. The bright galaxy itself is extremely red, having $r - [3.6] \approx 5.7$. It could perhaps be the radio counterpart, but the large offset from the radio position would be difficult to explain.

If there are radio sources without IRAC counterparts, they are unlikely to be local galaxies (cf., Masci et al. 2001). Gruppioni, Oliver, & Serjeant (2001) suggested that radio sources with no counterparts in deep optical surveys are likely to be early-type galaxies at $z > 1$. However, the absence of an IRAC counterpart for these galaxies is difficult to explain. At $z = 1$, the IRAC $3.6 \mu\text{m}$ detection limit $0.7 \mu\text{Jy}$ corresponds to a stellar luminosity of order $10^9 L_\odot$, and such low luminosity galaxies are unlikely to harbor powerful radio sources. Even at $z = 5$, a galaxy with $L = 10^{11} L_\odot$ should have been detected at $4.5 \mu\text{m}$. Any radio sources without IRAC counterparts are thus either less luminous or more distant than these limits.

⁵Source 9 has full-depth IRAC coverage. Upper limits for a counterpart coincident with the radio peak are $0.9 \mu\text{Jy}$ at 3.6 and $4.5 \mu\text{m}$ and $6 \mu\text{Jy}$ at 5.8 and $8 \mu\text{m}$, 5σ . Source 15 is closer to the edge of the IRAC coverage; exposure time is about 1/3 normal at 3.6 and $5.8 \mu\text{m}$ and about 60% of normal at 4.5 and $8.0 \mu\text{m}$ with detection limits correspondingly higher.

⁶This position has full-depth IRAC coverage.

4. Discussion

Spectral energy distributions (SEDs) indicate the type of galaxy and likely redshift range. Apparent magnitude is also a good distance indicator for radio galaxies (e.g., Fig. 1 of van Breugel et al. 1999). Fig. 3 shows an IRAC color-magnitude diagram for the radio source counterparts. There are two distinct groups of galaxies. One group, the “blue clump,” is brighter than $[8.0] = 15.8$ and quite blue ($[3.6] - [8.0] < 1.1$). A second group follows a distinct “stripe” from faint and blue to bright and red. Similar, though less distinct, separations are present in other C-M diagrams.

Eight of the radio source counterparts have distinct power law SEDs (Fig. 4): nearly a straight line in the log-log plot. (Davis et al. 2006 describe the BRI data used in the SED plots.) All these sources have spectral index $\alpha < 0$ ($F_\nu \propto \nu^\alpha$). Such SEDs are signatures of powerful AGN or QSOs (e.g. Elvis et al. 1994). Two of these galaxies are confirmed spectroscopically as broad-line AGN (Table 3); there are no spectra for the other six. All eight of the power-law galaxies are red in the $[3.6] - [8.0]$ color and fall along the “stripe” in the C-M diagram with the brightest AGN being the reddest. This may represent the combined effects of AGN luminosity and galaxy distance. Luminous, nearby AGN have little contribution from starlight at $8 \mu\text{m}$ and are therefore bright and red. Less luminous AGN are fainter, and the greater contribution of starlight relative to the AGN makes the color bluer. More distant AGN are also fainter, but because the observed radiation emerged at shorter wavelength in the galaxy’s rest frame, starlight makes a bigger contribution than for nearby galaxies.

Two other galaxies occupy the stripe region of the C-M diagram along with the AGN. One of them (#2) is a component of a dusty, interacting system. The infrared component corresponding to the radio source has a near power-law SED (Fig. 5) but with an upturn at $3.6 \mu\text{m}$. This component could be an AGN with contribution from starlight at the shortest wavelength. Fig. 2 shows thumbnail images of this source.

The other source in the stripe, #37, is unusual. It is easily detected in all IRAC bands with a flat SED (Fig. 5), but it is invisible on I-band HST images ($I > 26.8$, $0.04 \mu\text{Jy}$). The source is bright at $24 \mu\text{m}$ and has the second-highest radio flux density in the survey. One possibility is that #37 is a dusty galaxy at $2 \lesssim z \lesssim 3$, consistent with the $[3.6] - [4.5]$ color and the $1.6 \mu\text{m}$ stellar emission peak being observed near $5 \mu\text{m}$ (Fig. 5). The observed $24 \mu\text{m}$ would then come from the PAH emission features at rest $6-8 \mu\text{m}$, and the faint V and I magnitudes could be attributed to a combination

of the Balmer spectral break and heavy dust reddening. Higdon et al. (2005) reported finding four radio sources with similar $24\ \mu\text{m}$ flux densities and upper limits in visible light, but #37 has much higher radio flux density than any of the Higdon et al. sources. Houck et al. (2005) gave redshifts for 17 $R > 24.5$ MIPS sources, but only one would have been detectable in our radio survey. That source (their #13 at $z = 1.95$) is ten times brighter at $24\ \mu\text{m}$ but perhaps eight times fainter at 6 cm (guessing a radio spectral index of -0.7) than our #37. An alternative possibility is that #37 could be similar to extreme radio galaxies reported by van Breugel et al. (1999) and Waddington et al. (1999). If the intrinsic $K - [3.6]$ color is not extreme and the usual magnitude-redshift relation (van Breugel et al. 1999) applies, the magnitude $[3.6] = 17.9$ suggests $z \approx 2$ but is consistent with redshift as large as 5.

The galaxies in the “blue clump” in the color-magnitude diagram are all well above the sensitivity limit of the IRAC data. Waddington et al. (2000) identified counterparts of radio galaxies found at 1.4 GHz and found a peak in $2.2\ \mu\text{m}$ number counts at $K \approx 16$. This peak almost certainly represents the same population as the blue clump, but Waddington et al. could say little about these galaxies without data at longer wavelengths. The blue clump galaxies have SEDs consistent with normal galaxies (Figs. 6–8). The color-color diagrams in Figs. 9 and 10 compare these galaxies to the colors of typical spiral and elliptical galaxies. Most of the galaxies have $0.5 < z < 1$ as indicated by the color tracks in Figs. 9 and 10, primarily the $[3.6] - [4.5]$ color. The $3.6\ \mu\text{m}$ magnitudes of the blue clump galaxies range from 14.5 to 16.5, consistent with the redshift- K relation (van Breugel et al. 1999) for $0.5 < z < 1$ and the expected $K - [3.6] \approx 0.5$ at these redshifts. If $z > 0.5$, and assuming a radio spectral index not far from the usual -0.7 , the radio power emitted at 1.4 GHz is $> 10^{24}\ \text{W Hz}^{-1}$. Such high radio luminosity indicates an AGN, consistent with the findings of Hammer et al. (1995) and Mobasher et al. (1999) in their radio surveys. Benn et al. (1993) found a much larger fraction of star-forming galaxies, but their data apply to fainter radio flux densities and brighter optical magnitudes, hence lower redshifts, than the sources studied here. The absence of an obvious power law emission component in the mid-infrared implies that the active nucleus is either obscured or has such low luminosity that it does not dominate the near infrared SED of the galaxy. Barmby et al. (2006) found that 60% of X-ray selected AGN also lack a dominant mid-IR power law component. No doubt similar galaxies exist at larger redshifts than are detected here, but they are below the detection limit of the radio survey because of the strong K-correction as well as inverse-square dimming.

The galaxy classes separated in the color-magnitude diagram also show different

ratios of radio to near-infrared flux density. Fig. 11 shows that for a given radio flux density, the blue clump galaxies tend to be brighter at $3.6\ \mu\text{m}$ than the stripe galaxies. Georgakakis et al. (1999, their Fig. 12) found that the radio sources with the highest flux densities (which are the only ones our survey could have detected) tended to be AGN and absorption systems (i.e., ellipticals) rather than star-forming galaxies. Presumably the radio emission comes from an AGN in these types. Masci et al. (2001) also found radio emission larger than expected from star formation alone in their radio sample. If radio flux density indicates “AGN power,” Fig. 11 suggests that the clump galaxies contain a large stellar population that outshines the underlying AGN. Further observations (and in particular redshifts) will be needed to determine whether the “blue clump” and “stripe” populations differ in fundamental ways or are simply the result of varying ratios of AGN to stellar light.

Photometric classification of galaxies is an uncertain business at best, but Figs. 9 and 10 show there is a tendency for more blue-clump galaxies to fall close to the elliptical than the spiral colors. The colors also provide very rough photometric redshifts. Figs. 6 and 7 illustrate the SEDs. In all cases where DEEP2 spectroscopy is available, it confirms the photometric classifications.⁷ The spectra exhibit three main classes:

1. An old stellar population (labelled “old” in Table 3). These galaxies show calcium H and K lines in absorption and often the G band, consistent with high luminosity, early-type galaxies. A few of these galaxies show weak [O II] emission lines indicative of some recent star formation or LINER activity, but the $U - B$ colors are red (≥ 0.33), suggesting that the star formation or nuclear activity has had little effect on the bulk of the stellar population. Of the ten galaxies in Fig. 6, the six that have spectra are all of old type.
2. Three galaxies show strong Balmer absorption lines typical of A stars; these galaxies are labelled “post-SB” (post-starburst) in Table 3. All three are in the blue clump and have colors resembling the spiral template. (See Fig. 7.) One of the three galaxies (#39/40) also shows [Ne V] emission lines characteristic of AGN. Its SED shows a rise at $8\ \mu\text{m}$, which may be the signature of a power-law spectral component.

⁷Most of the spectra were not yet available when the photometric classifications were made, so this is not a case of “knowing the answer in advance.”

3. Three galaxies show AGN emission lines. Two with broad emission lines show power law SEDs (Fig. 4), and the third is #39/40 mentioned above.

Appendix A gives details of all the spectra. The apparent numbers of ellipticals and spirals are consistent with previous results (Georgakakis et al. 1999; Gruppioni, Mignoli, & Zamorani 1999; Ciliegi et al. 2003; Richards et al. 1998; Chapman et al. 2003). The prevalence of early-type, i.e., not star forming, galaxies adds weight to our suggestion that the radio sources arise from active nuclei, not starbursts. Despite the good agreement between photometry and spectra as regards galaxy type, there is one discrepancy in the redshift order. Source 3 has a higher redshift than #22 according to color, but spectroscopy shows the opposite. This should serve as a warning to be cautious about classifications or redshifts derived from limited photometry. Nevertheless, the spectroscopic redshifts confirm the general redshift range $0.5 \lesssim z \lesssim 1.0$ derived from colors and magnitudes.

Another indicator of nuclear activity is X-ray emission (Mushotzky 2004). Published X-ray observations with Chandra (Nandra et al. 2005) and XMM-Newton (Waskett et al. 2003) cover part of the EGS (Barmby et al. 2006). Six radio sources are within the area covered by both Chandra and XMM: four (EGS06 14/22/23/24) are not detected in X-rays. Source 19 is coincident with Chandra source 83 but is not detected by XMM; source 21 coincides with Chandra source 55 and XMM source 53. Eight radio sources (eleven components) are within the area covered by XMM alone: six (EGS06 12/13/15/17/18/20/26/27) are not detected in X-rays, but EGS06 10/11 and 16 are coincident with XMM sources 5 and 43, respectively. The X-ray/radio coincidence rate is therefore 4/14, or 29%. EGS06 10/11 has the highest radio flux density in the sample and is a definite AGN from its SED. The other three X-ray-detected sources are clump sources with no obvious distinction from the other clump sources except that #16 shows modest excess emission at $8 \mu\text{m}$ that might be attributed to an AGN power law. The ratio of $24 \mu\text{m}$ flux density to soft X-ray flux puts all four X-ray sources into the AGN category by an order of magnitude (Weedman, Charmandaris, & Zezas 2004; $IR/X < 0.05$ in their units). EGS06 10/11 and 23 are the only radio sources in the X-ray area whose IRAC SEDs are AGN-like. A possible explanation for the X-ray non-detection of 23 is obscuration, as found by Donley et al. (2005) for “radio-excess AGN.” Detection of radio sources that are likely to be AGN yet do not show X-ray emission is additional evidence that no single-wavelength survey can produce a complete list of AGN.

5. Conclusions

IRAC images are a powerful means of identifying and classifying radio sources. Deep IRAC images identify counterparts to at least 92% and possibly 100% of ~ 0.5 mJy radio sources. Many of the counterparts have very red visible to mid-infrared colors, underscoring the difficulty of identification at shorter wavelengths. The radio sources are likely to arise from powerful AGN, but only about 25% show a typical AGN power-law component that dominates the mid-infrared emission. For about 70% of the counterparts, galaxy starlight dominates the mid-infrared emission. The starlight-dominated galaxies can be identified by their blue [3.6] – [8.0] IRAC colors. These “blue clump” galaxies show a small range of apparent magnitude, suggesting a relatively small range of redshift for this galaxy type in this survey. The small range is probably a combination of the radio survey sensitivity limit and relative rarity at low redshift of galaxies hosting powerful radio sources. The separation into “stripe” and “blue clump” galaxies should be useful in classifying galaxies found in other radio surveys.

We thank Jeff Newman and the DEEP team for access to the Keck spectroscopic data. This work is based in part on observations made with the Spitzer Space Telescope, which is operated by the Jet Propulsion Laboratory, California Institute of Technology under a contract with NASA. Support for this work was provided by NASA through an award issued by JPL/Caltech. The National Radio Astronomy Observatory is a facility of the National Science Foundation operated under cooperative agreement by Associated Universities, Inc. A.L.C. acknowledges support by NASA through Hubble Fellowship grant HF-01182.01-A, awarded by the Space Telescope Science Institute, which is operated by the Association of Universities for Research in Astronomy, Inc., for NASA, under contract NAS 5-26555. DEEP spectroscopy is supported by the National Science Foundation grants AST-0071198 and AST-0507483.

Facilities: VLA Spitzer/IRAC Spitzer/MIPS Keck Subaru

A. Details of DEEP2 Visible Spectra

Spectra are all of good quality. Whenever the [O II] doublet is seen with good S/N, the lines have velocity widths too broad for a clean separation of the doublet

components, which are 220 km s^{-1} apart. The implied large internal kinematics are consistent with the prevailing view that radio sources are hosted by a massive galaxies.

For each object that has a spectrum, the DEEP2 catalog number, mask, and slit identifications are listed in parentheses followed by a brief description of the spectrum. Objects are identified by their EGS06 numbers as given in Tables 1 and 3.

3: (11021233, mask 1101, slit 111) Absorption spectrum characteristic of old population shows Ca HK, H δ , G band, H β , and Mg b.

19: (12007962, mask 1245, slit 85) The absorption line spectrum showing Ca HK is consistent with an old stellar population; moderate-strength [O II] emission is also seen.

21: (12012467, mask 1243, slit 88) Moderate strength [O II] is seen along with moderately strong Balmer absorption lines of H δ and H γ . Spectral type is between an old and post-starburst stellar population.

22: (12012898, mask 1205, slit 107) Excellent match to an old stellar population template through H β and [O III]; [O II] emission is visible but of too low S/N to estimate a velocity width.

24: (12016405, mask 1209, slit 72) Excellent match to an old stellar population template from Ca H through Mg b; [O II] is out of spectral range.

28: (12020403, mask 1210, slit 97) AGN signatures are seen with Mg II, [Ne V], and [O II] all in emission and broad. Two sets of strong Mg II absorption are superimposed with one that is close to the redshift defined by the [O II] emission line and another that is shifted to the red (perhaps from infalling gas) by about 300 km s^{-1} . There is also a "foreground" Mg II absorption doublet seen at redshift $z=1.38$; candidates for its source may be among galaxies seen in the field at separations of about 3".

30: (13004312, mask 1300, slit 73) Good match to a pure absorption-line old stellar population over the wavelength range from near H β through H α .

36: (13025514, mask 1309, slit 49) Excellent match to a pure old stellar population over the wavelength range from the G band through Na I. Faint continuum of another spectrum $\sim 2''$ away shows a slight absorption at the G band. Being at the same redshift as that of the radio galaxy, this feature suggests that we may be watching a minor merger.

44: (13058191, mask 1315, slit 121) Excellent S/N continuum shows unusually strong Balmer absorption indicative of a post-starburst. [O II] is outside the spectral range, and the red end is past Mg b. H β and H γ emission lines are also seen; they appear tilted in the 2-D spectrum and are spatially asymmetric. Moreover, the H β emission is redshifted by several 10's of km s $^{-1}$ with respect to its absorption, consistent with a possible inflow of ionized gas. [O III] lines are not seen. The r image shows no companions within 3".

10/11: (11045619, mask 1114, slit 83) The spectrum has broad emission lines of Mg II and [Ne V], as well as strong Mg II and Mg I in absorption. If the emission lines of [Ne V] are used as a reference, these absorption lines of Mg II show a redshift by 150 km s $^{-1}$, while a much weaker set of Mg II absorption lines appear with a blueshift of over 500km/s.

39/40: (13032337, mask 1313, slit 30) The spectrum has excellent S/N and shows unusually strong Balmer absorption lines that are characteristic of post-starbursts. Strong [Ne V] emission lines at 3345Å and 3426Å characteristic of AGN along with strong [O II] are also detected with velocity dispersions of about 200 km s $^{-1}$. This AGN/starburst spectrum is flanked by two other spectra a few arcsecs away and at slightly lower redshifts by about 100 km s $^{-1}$. One shows narrow (unresolved) emission lines of [O II], H δ , and H γ , while the other shows broader lines ($\sigma \approx 200$ km s $^{-1}$) of [O II] and [Ne III]. Yet another flanking feature is weak detection of [O II] emission at redshift z=1.42, presumably from a background (possibly lensed) galaxy. The r image shows at least four other galaxies at separations \gtrsim 3".

REFERENCES

Barmby, P., et al. 2006, *ApJ*, 642, 126

Baum, W. A. 1957, *AJ*, 62, 6

Bell, E. F., & de Jong, R. S. 2001, *ApJ*, 550, 212

Benn, C. R., Rowan-Robinson, M., McMahon, R. G., Broadhurst, T. J., & Lawrence, A. 1993, *MNRAS*, 263, 98

Blake, C., & Bridle, S. 2005, *MNRAS*, 363, 1329

Chapman, S. C., et al. 2003, *ApJ*, 585, 57

Ciliegi, P., Gruppioni, C., McMahon, R., & Rowan-Robinson, M. 2001, *Ap&SS*, 276, 957

Ciliegi, P., Zamorani, G., Hasinger, G., Lehmann, I., Szokoly, G., & Wilson, G. 2003, *A&A*, 398, 901

Ciliegi, P., et al. 2005, ArXiv Astrophysics e-prints, arXiv:astro-ph/0506690

Coil, A. L., Newman, J. A., Kaiser, N., Davis, M., Ma, C.-P., Kocevski, D. D., & Koo, D. C. 2004, *ApJ*, 617, 765

Condon, J. J., Cotton, W. D., Greisen, E. W., Yin, Q. F., Perley, R. A., Taylor, G. B., & Broderick, J. J. 1998, *AJ*, 115, 1693

Davis, M., et al. 2003, *Proc. SPIE*, 4834, 161

Davis, M., et al. 2006, *ApJ*, in press.

Donley, J., Rieke, G. H., Rigby, J. R. & Pérez-González, P. G. 2005, *ApJ*, in press (astro-ph/0507676)

Elvis, M., et al. 1994, *ApJS*, 95, 1

Fazio, G. G., et al. 2004, *ApJS*, 154, 10

Fazio, G. G., et al. 2004, *ApJS*, 154, 39

Fomalont, E. B., Windhorst, R. A., Kristian, J. A., & Kellerman, K. I. 1991, *AJ*, 102, 1258 (FWKK)

Georgakakis, A., Mobasher, B., Cram, L., Hopkins, A., Lidman, C., & Rowan-Robinson, M. 1999, MNRAS, 306, 708

Gonzalez-Solares, E. A., et al. 2005, MNRAS, 358, 333

Gruppioni, C., Mignoli, M., & Zamorani, G. 1999, MNRAS, 304, 199

Gruppioni, C., Oliver, S., & Serjeant, S. 2001, Ap&SS, 276, 791

Gruppioni, C., Pozzi, F., Zamorani, G., Ciliegi, P., Lari, C., Calabrese, E., La Franca, F., & Matute, I. 2003, MNRAS, 341, L1

Hammer, F., Crampton, D., Lilly, S. J., Le Fevre, O., & Kenet, T. 1995, MNRAS, 276, 1085

Higdon, J. L., et al. 2005, ApJ, 626, 58

Helou, G., Soifer, B. T., & Rowan-Robinson, M. 1985, ApJ, 298, L7

Houck, J. R., et al. 2005, ApJ, 622, L105

Hopkins, A., Afonso, J., Cram, L., & Mobasher, B. 1999, ApJ, 519, L59

Ivison, R. J., Chapman, S. C., Faber, S. M., Smail, I., Biggs, A. D., Conselice, C. J., Wilson, G., Salim, S., Huang, J.-S., & Willner S. P. 2006, ApJ, submitted.

Masci, F. J., et al. 2001, PASP, 113, 10

Minkowski, R. 1960, ApJ, 132, 908

Mobasher, B., Cram, L., Georgakakis, A., & Hopkins, A. 1999, MNRAS, 308, 45

Mushotzky, R. 2004, in ASSL Vol. 308: Supermassive Black Holes in the Distant Universe, ed. A. Barger (Kluwer Academic, Dordrecht), 53

Nandra, K., Laird, E. S., Adelberger, K., Gardner, J., Mushotzky, R. F., Rhodes, J., Steidel, C. C., Teplitz, H. I., & Arnaud, K. A. 2005, MNRAS, 356, 568

Norris, R. P., et al. 2001, Deep Fields, Proc. ESO/ECF/STScI Workshop, Springer, p. 135

Reach, W. T., et al. 2005, PASP, 117, 978

Richards, E. A., Kellermann, K. I., Fomalont, E. B., Windhorst, R. A., & Partridge, R. B. 1998, AJ, 116, 1039

Schinnerer, E., et al. 2004, AJ, 128, 1974

Spinrad, H., Marr, J., Aguilar, L., & Djorgovski, S. 1985, PASP, 97, 932

Stern, D. et al. 2005, ApJ, in press.

van Breugel, W., De Breuck, C., Stanford, S. A., Stern, D., Röttgering, H., & Miley, G. 1999, ApJ, 518, L61

van der Laan, H., Katgert, P., Windhorst, R., & Oort, M. 1983, IAU Symp. 104: Early Evolution of the Universe and its Present Structure, 104, 73

Vogt, N. P., et al. 2005, ApJS, 159, 41

Waddington, I., Windhorst, R. A., Cohen, S. H., Partridge, R. B., Spinrad, H., & Stern, D. 1999, ApJ, 526, L77

Waddington, I., Windhorst, R. A., Dunlop, J. S., Koo, D. C., & Peacock, J. A. 2000, MNRAS, 317, 801

Weskett, T. J., Eales, S. A., Gear, W. K., Puchnarewicz, E. M., Lilly, S., Flores, H., Webb, T., Clements, D., Stevens, J. A., & Thuan, T. X. 2003, MNRAS, 341, 1217

Weedman, D., Charmandaris, V., & Zelaz, A. 2004, ApJ, 600, 106

Windhorst, R. A. 1986, Highlights in Astronomy, 7, 355

Yun, M. S., Hibbard, J. E., Condon, J. J., & Reddy, N. 1999, Ap&SS, 266, 29

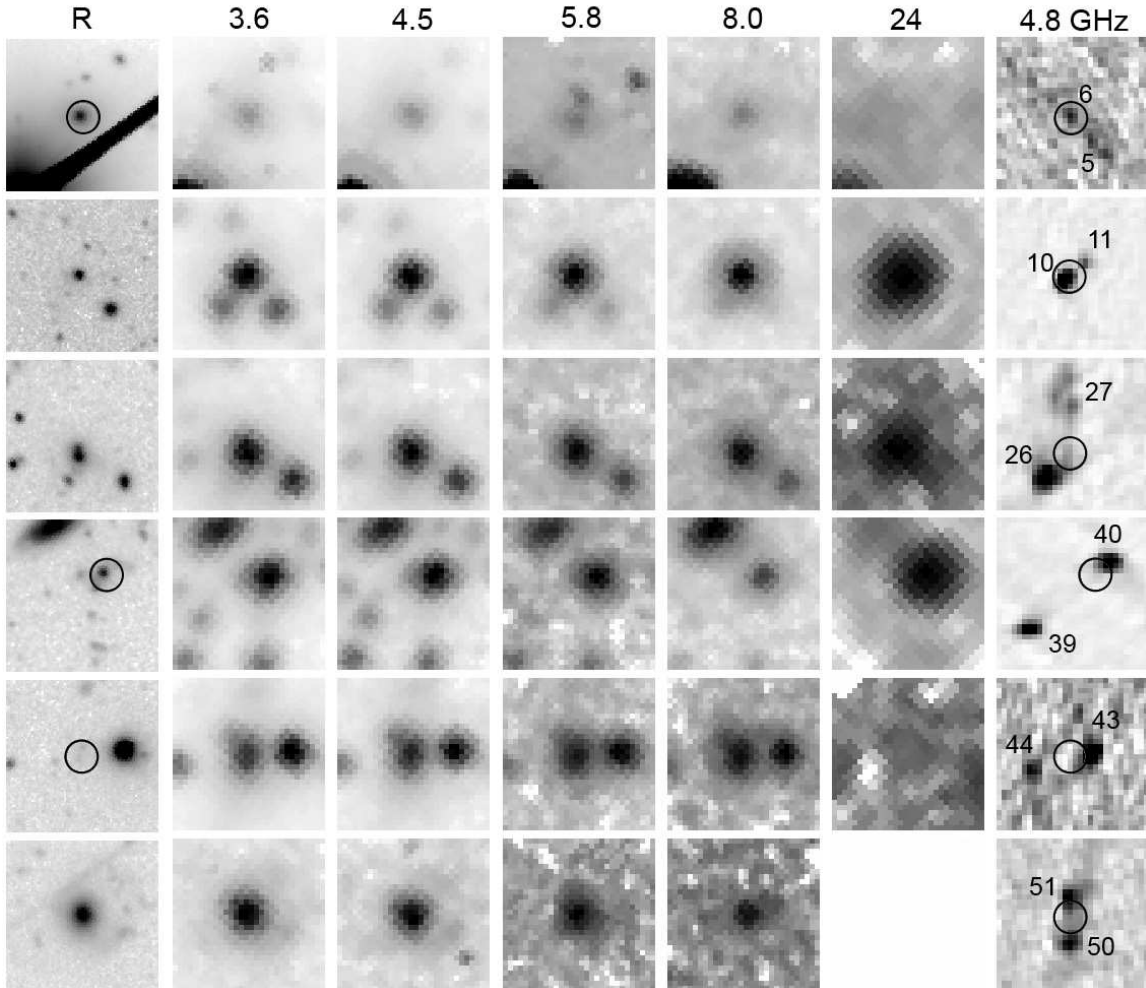


Fig. 1.— Thumbnail images of possible double radio sources. Shown left to right are Subaru r , IRAC 3.6, 4.5, 5.8, and 8.0 μm , MIPS 24 μm , and VLA 4.8 GHz. Each thumbnail is 18'' on a side with north up and east to the left. Greyscale is negative square root except for the radio images, which are negative linear. Circles show the location of 5.2'' photometry apertures. EGS06 50/51 are outside the MIPS 24 μm coverage.

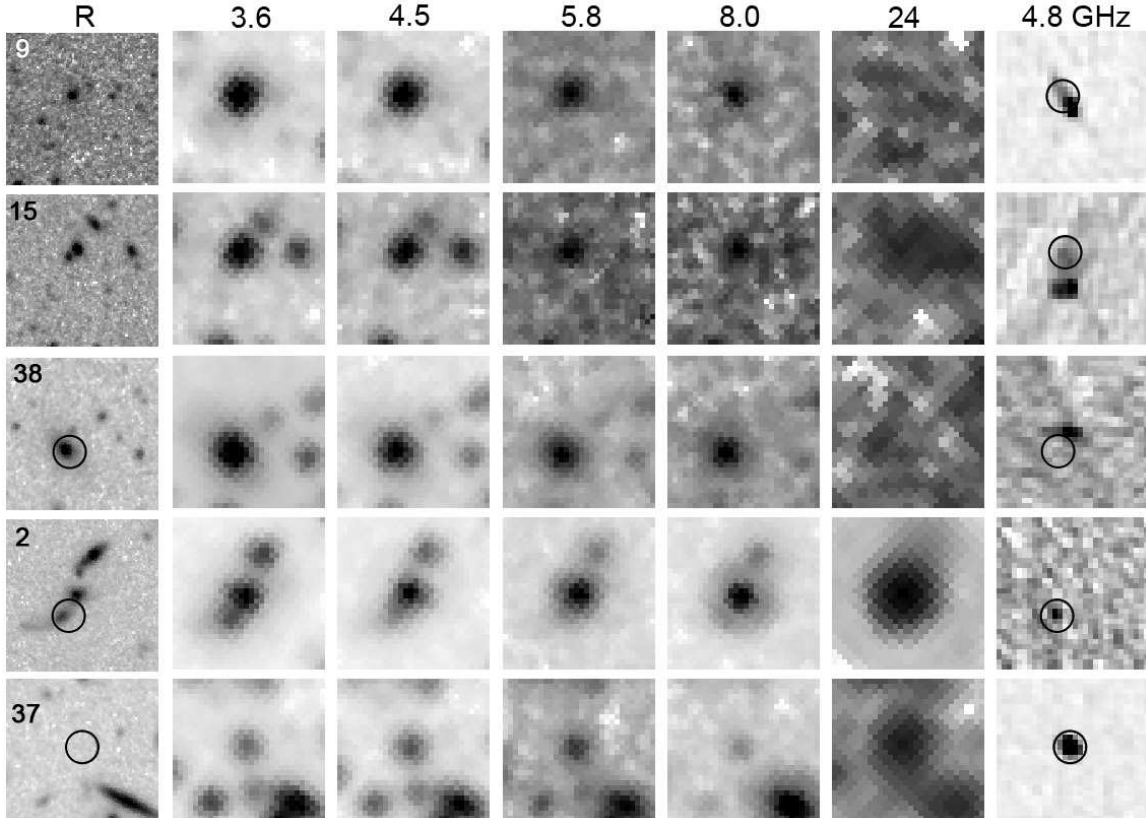


Fig. 2.— Thumbnail images of radio source areas. Image details are the same as Fig. 1. The top three rows show the regions of three radio sources considered unidentified. Bottom two rows show interesting identified sources. Circles show the location of the $5.2''$ photometry apertures, the nearest IRAC source in the case of the three unidentified radio sources. The image of EGS06 2 is centered on the brightest IRAC component at $14:14:33.16 +52:02:55.3$ (J2000).

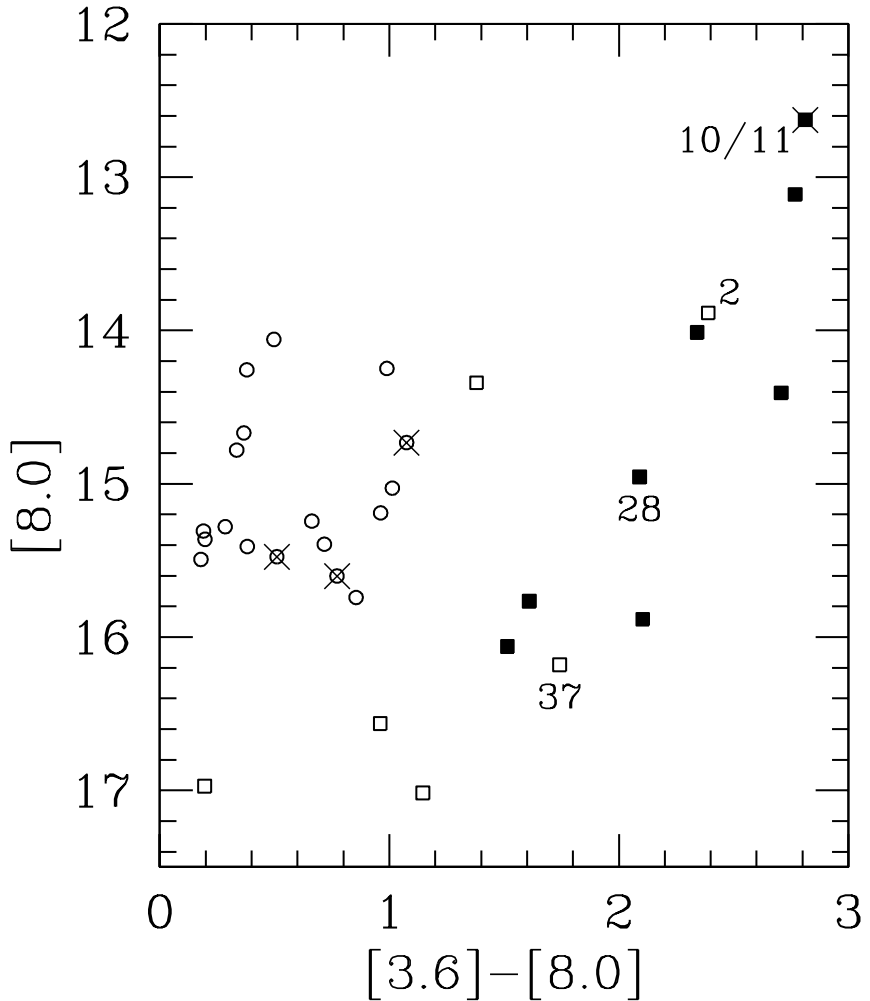


Fig. 3.— Color-magnitude diagram for IRAC counterparts of radio sources. Filled symbols indicate galaxies classified as AGN because they have power-law SEDs. Symbols with superposed x indicate the four detected X-ray sources. The “blue clump” refers to the group of sources with $[8.0] < 16$ and $[3.6] - [8.0] < 1.2$, indicated with open circles. Four objects discussed in the text are identified with numbers from Table 3. The 5σ sensitivity limit is $[8.0] = 17.55$; sensitivity at $3.6 \mu\text{m}$ does not limit detection of sources plotted here.

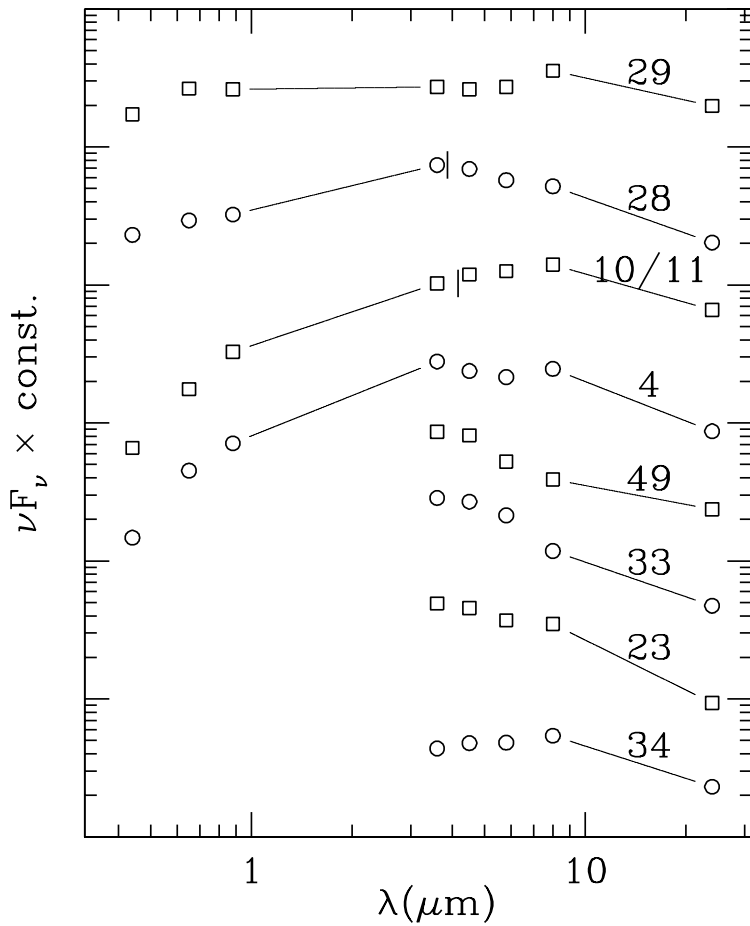


Fig. 4.— SEDs for eight galaxies showing power law SEDs and thus classified AGN. Wavelengths are in the observed frame; vertical lines show rest $1.6 \mu\text{m}$ for galaxies having spectroscopic redshifts. Symbol types alternate for clarity. Lines bridge wavelength gaps in the observations and should not be taken to suggest the actual SED. Photometric error bars are smaller than the symbol sizes in this and subsequent SED plots.

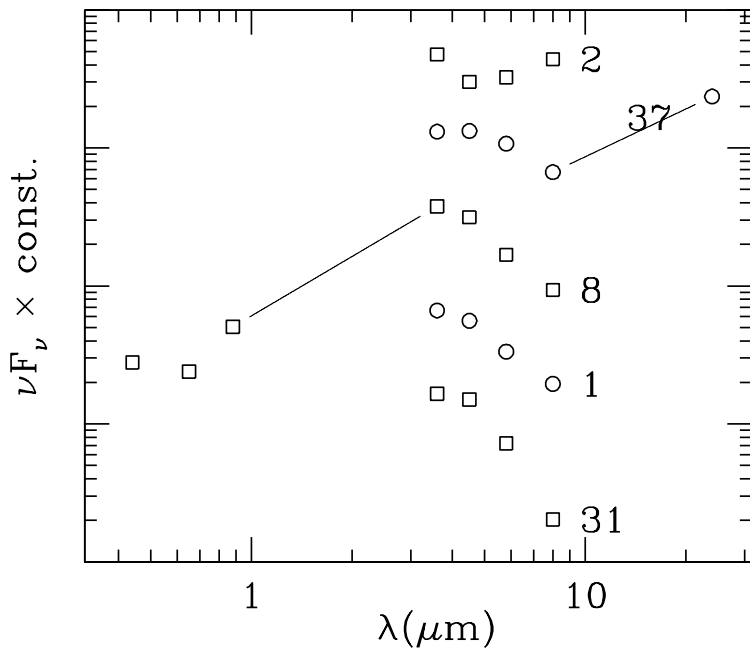


Fig. 5.— SEDs for five galaxies in the stripe of the C-M diagram but not having power law SEDs. Wavelengths are in the observed frame; none of these galaxies has a spectroscopic redshift. For EGS06 2, the data shown are for only the single component shown in Fig. 2, not for the entire system. Symbol types alternate for clarity. Lines bridge wavelength gaps in the observations and should not be taken to suggest the actual SED.

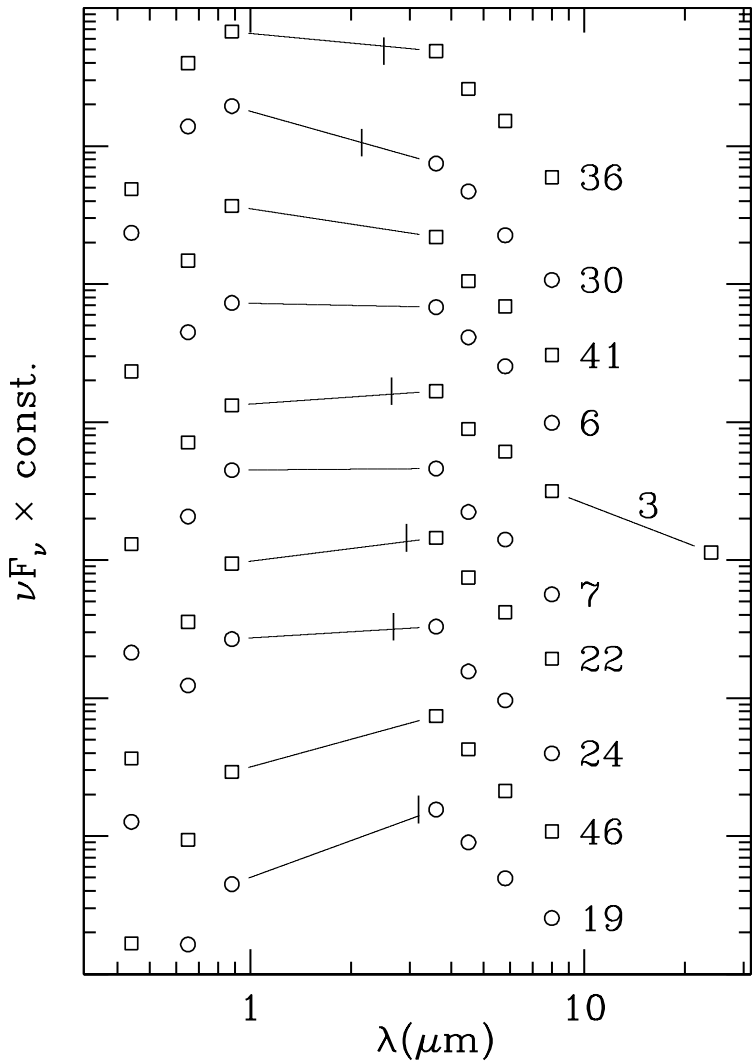


Fig. 6.— SEDs for ten blue clump galaxies having colors most resembling the elliptical template in Fig. 9. Symbol types alternate for clarity. Wavelengths are in the observed frame; vertical lines show rest $1.6 \mu\text{m}$ for galaxies having spectroscopic redshifts. Symbol types alternate for clarity. Lines bridge wavelength gaps in the observations and should not be taken to suggest the actual SED.

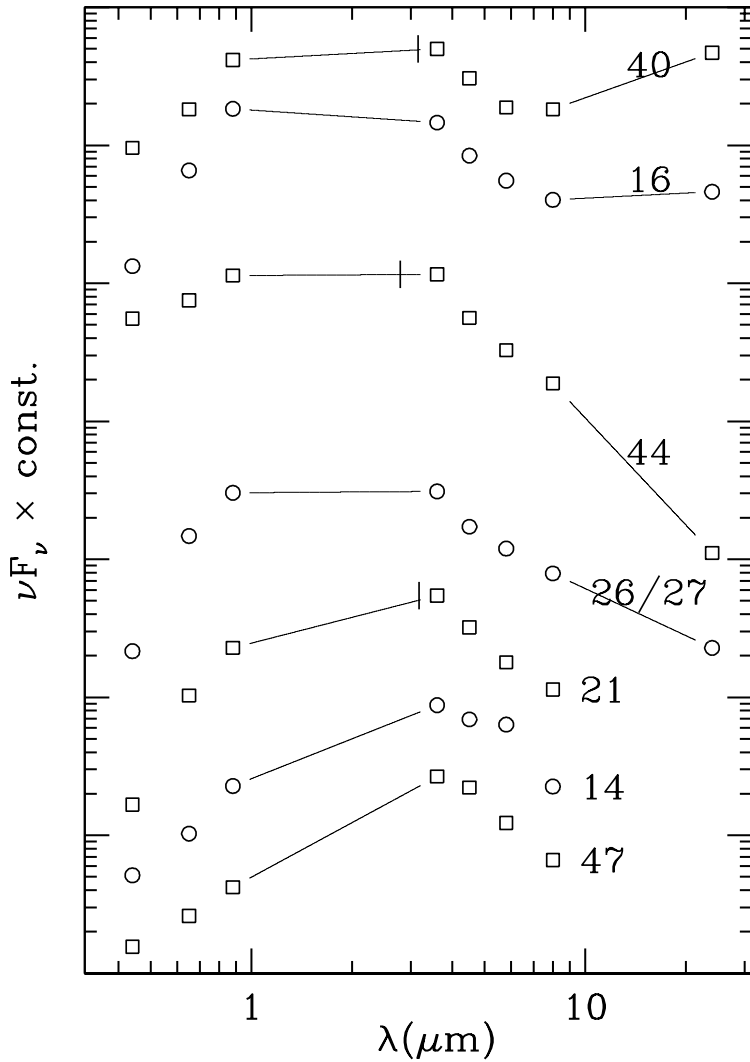


Fig. 7.— SEDs for six blue clump galaxies having colors most resembling the spiral template in Fig. 9. Symbol types alternate for clarity. Wavelengths are in the observed frame; vertical lines show rest $1.6 \mu\text{m}$ for galaxies having spectroscopic redshifts.

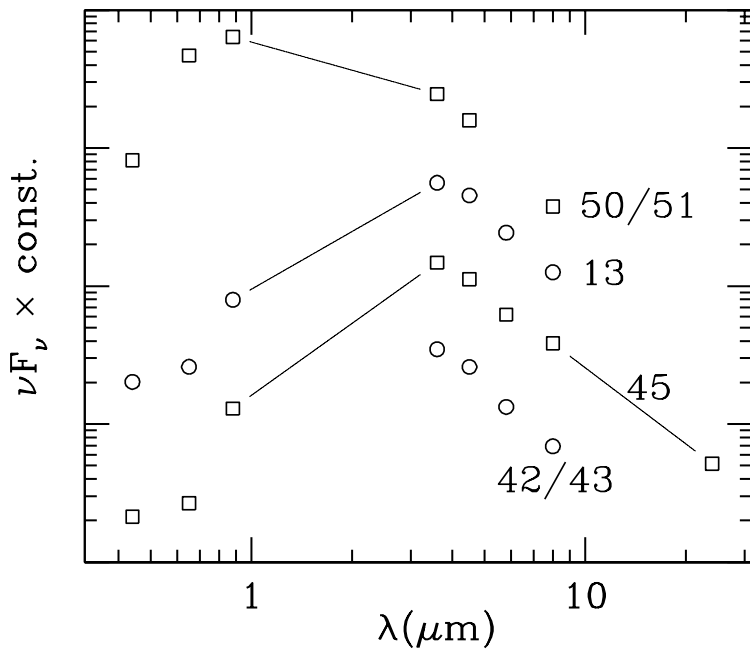


Fig. 8.— SEDs for four blue clump having colors that cannot distinguish a likely morphological type. Red [3.6] – [4.5] colors suggest $z > 1$ for all. Symbol types alternate for clarity. Lines bridge wavelength gaps in the observations and should not be taken to suggest the actual SED. Wavelengths are in the observed frame; none of these galaxies has a spectroscopic redshift.

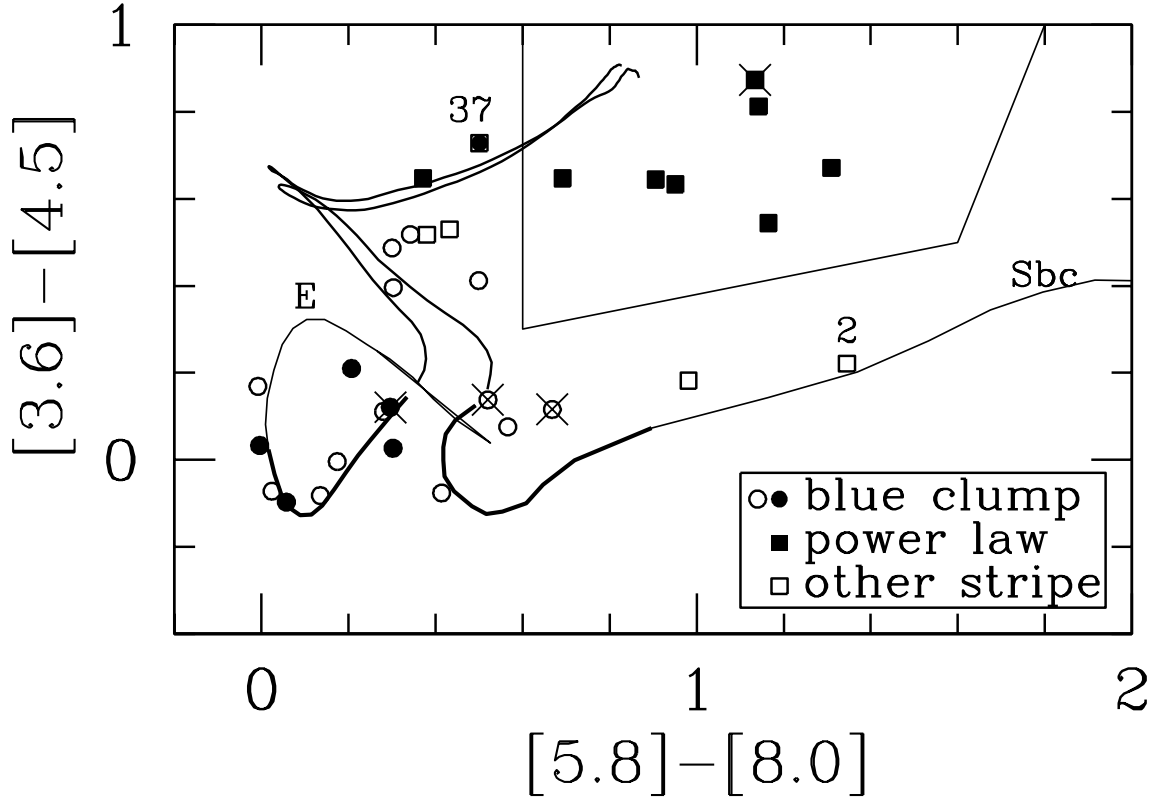


Fig. 9.— Color-color diagram for IRAC counterparts of radio sources. Circles indicate galaxies in the blue clump; filled circles indicate blue clump galaxies with spectra that show an old stellar population. Filled squares indicate galaxies classified as AGN because they have power-law SEDs. Open squares indicate the remaining galaxies in the stripe; they have color/magnitude combinations outside the blue clump but not power law SEDs. X-ray sources are marked with a superposed x. Curved lines show colors of typical Sbc and E galaxies as a function of redshift from $z = 0$ to $z = 4$; curves are labelled near the low-redshift end. The heavy portion of each track indicates $0.5 < z < 1$, and $z = 4$ is at the top of the diagram. The color tracks show PAH emission shifting out of the IRAC 8 μm band as redshift increases from 0 to 0.5 and the 1.6 μm peak of the stellar energy distribution shifting through the IRAC bands as redshift increases. Thin, straight lines indicate the area Stern et al. (2005) found for the colors of spectroscopically-identified AGN. Objects with uncertain photometry as indicated in Table 4 are omitted, and two objects of interest are labeled.

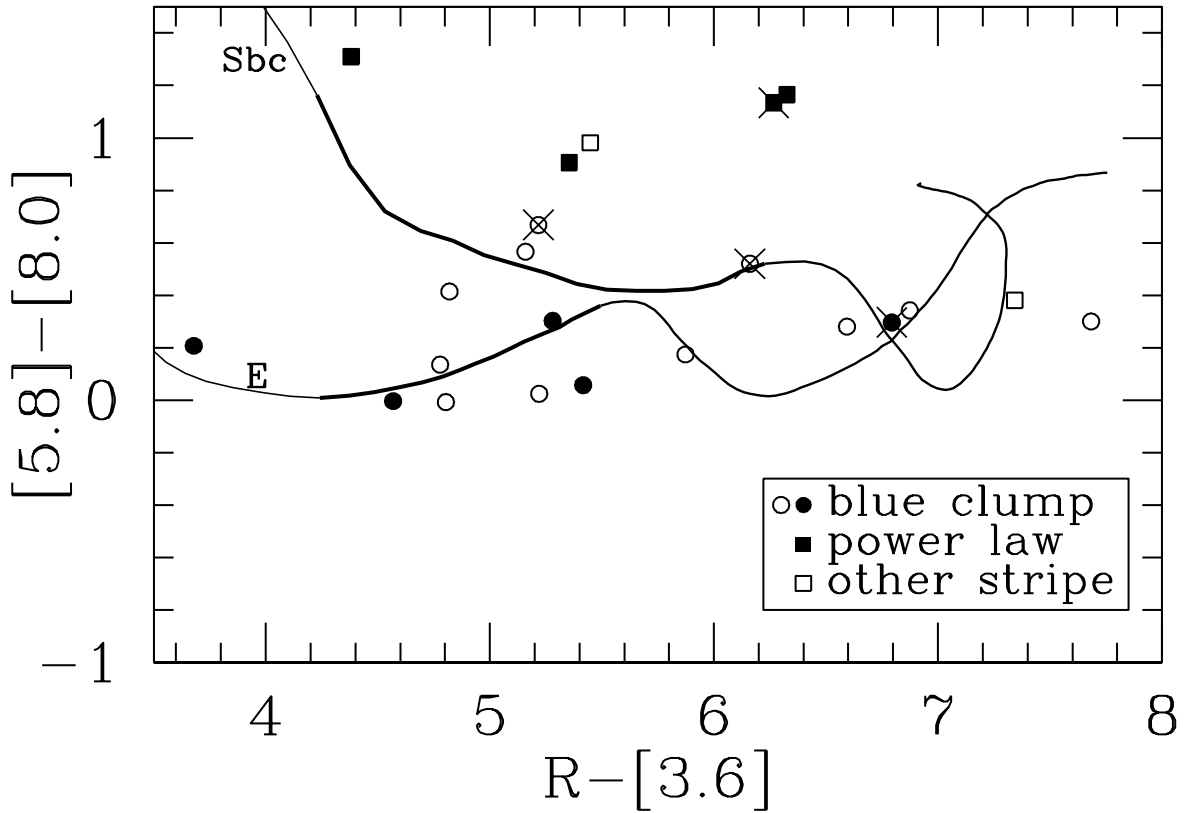


Fig. 10.— Color-color diagram for IRAC counterparts of radio sources. Circles indicate galaxies in the blue clump, and filled circles indicate blue clump galaxies with spectra that show an old stellar population. Filled squares indicate galaxies classified as AGN because they have power-law SEDs. Open squares indicate the remaining galaxies, which have color/magnitude combinations outside the blue clump but not power law SEDs. X-ray sources are marked with a superposed x. Curved lines show colors of Sbc (red $[5.8] - [8.0]$ color) and E galaxies as a function of redshift from low redshift to $z = 4$. The heavy portion of each track indicates $0.5 < z < 1$, and tracks are labelled near $z = 0.5$. Objects with uncertain photometry as indicated in Table 4 are omitted. The red colors of many of the counterparts suggest high redshifts and underscore the difficulty of detecting counterparts in visible-wavelength images. The object with $R - [3.6] < 4$ is #30 at $z = 0.346$.

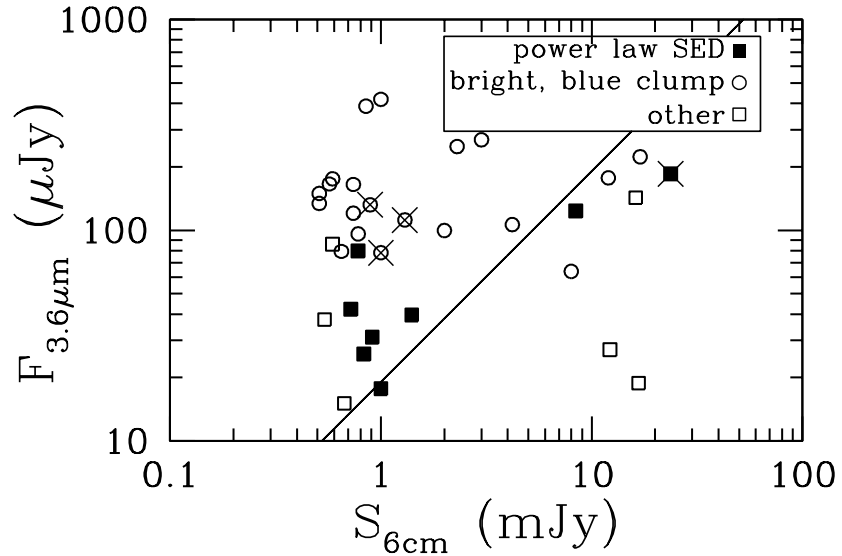


Fig. 11.— Comparison of $3.6 \mu\text{m}$ and radio flux densities. Filled symbols indicate galaxies classified as AGN because they have power-law SEDs. Open circles indicate galaxies in the blue clump. Open squares indicate the remaining galaxies, which have color/magnitude combinations outside the blue clump but not power law SEDs. X-ray sources are marked with a superposed x. The solid line shows the average ratio of $3.6 \mu\text{m}$ to radio flux density for radio loud quasars (Elvis et al. 1994, Fig. 10). Galaxies undetected at $3.6 \mu\text{m}$ would fall more than an order of magnitude below the bottom limit of this plot.

Table 1. EGS 6 cm Radio Sources

Name EGS06	RA J2000	Dec	PB corr	Stot mJy	Size(‘‘) maj min	Comments
Isolated sources						
1	14 15 03.92	52 01 06.5	1.14	0.67 ± .09		
2	14 14 33.36	52 02 53.1	1.12	0.59 ± .07		
3	14 14 36.75	52 05 03.1	1.02	0.74 ± .10	0.6 <0.3	
4	14 15 08.83	52 06 42.2	1.16	0.78 ± .12		
7	14 16 15.07	52 11 21.6	1.00	0.57 ± 0.1		
8	14 16 11.86	52 12 04.8	1.02	12.2 ± 0.1	0.6 <0.2	
9	14 15 36.84	52 14 09.7	1.15	10.9 ± 1.5	5.0 <1.0	pa 40°
12	14 16 08.06	52 24 58.5	1.24	3.2 ± 0.3	1.0 <0.5	outside IRAC area
13	14 16 21.88	52 25 03.3	1.06	8.0 ± 0.2	0.9 <0.3	
14	14 17 59.29	52 25 54.0	1.39	0.65 ± 0.2	0.6 <0.2	
15	14 16 30.12	52 27 01.1	1.15	9.0 ± 2	5.0 <1.0	peak flux position, extended to north
16	14 16 27.95	52 27 07.1	1.21	0.89 ± .14		
19	14 17 49.20	52 28 03.1	1.13	1.3 ± 0.2	1.1 <0.3	
20	14 16 23.30	52 28 27.2	1.41	1.1 ± 0.2		outside IRAC area
21	14 17 32.63	52 32 03.1	1.04	1.0 ± 0.2	1.9 <0.8	
22	14 17 13.59	52 32 13.8	1.07	0.74 ± .09		
23	14 18 09.95	52 33 00.2	1.19	1.0 ± 0.2	1.8 <0.5	
24	14 17 53.38	52 35 39.3	1.02	0.51 ± 0.07		
25	14 17 04.19	52 37 54.5	1.81	3.7 ± 0.5	1.3 <0.6	outside IRAC area
28	14 18 05.55	52 40 32.3	1.19	0.72 ± .19		
29	14 19 45.50	52 46 48.1	1.33	8.4 ± 0.2	0.3 <0.2	
30	14 19 10.40	52 48 30.7	1.14	3.0 ± 0.6	7.4 1.5	pa 49°
31	14 18 37.75	52 51 28.9	1.14	0.54 ± .09		
32	14 18 45.92	52 51 42.0	1.05	0.41 ± .08		outside IRAC area
33	14 19 46.17	52 56 47.2	1.20	0.83 ± 0.14	0.6 0.0	
34	14 20 50.34	52 57 46.9	1.44	1.4 ± 0.2	0.8 0.0	
35	14 21 01.41	52 57 55.4	1.55	0.87 ± 0.19		outside IRAC area
36	14 20 33.36	52 58 00.8	1.03	0.59 ± 0.12	0.5 0.0	
37	14 20 33.26	53 00 03.8	1.18	16.7 ± 0.16		
38	14 21 04.93	53 02 09.4	1.22	1.64 ± 0.25	1.8 1.1	
41	14 20 33.35	53 08 21.0	1.05	2.3 ± 0.14	0.8 0.1	
44	14 20 56.85	53 13 07.5	1.00	1.0 ± 0.12	1.0 0.4	
45	14 21 54.78	53 15 00.6	1.13	4.2 ± 0.09		
46	14 21 27.90	53 15 16.1	1.18	0.51 ± 0.1		

Table 1—Continued

Name	RA	Dec	PB	Stot	Size('')	Comments
EGS06	J2000		corr	mJy	maj min	
47	14 21 37.15	53 20 55.2	1.01	0.78 ± 0.17	1.5 0.8	
48	14 22 01.41	53 27 55.3	1.43	0.80 ± 0.14		outside IRAC area
49	14 23 12.71	53 27 56.7	1.07	0.91 ± 0.17	1.4 0.0	
Possible multiple sources						
5	14 14 53.00	52 10 25.2	1.19	1.5 ± 0.3	3.5 <0.6	size uncertain, outside IRAC area
6	14 14 53.35	52 10 29.0	1.19	0.85 ± 0.18	5.8 from 5, outside IRAC area	
10	14 16 22.85	52 19 15.9		21.7 ± 0.5	1.8 <0.6	classical double morphology,
11	14 16 22.56	52 19 18.0		4.4 ± 0.3	1.0 <1.0	3.1 separation
10 + 11 tot			1.05	26 ± 3		
17	14 16 25.55	52 27 14.4		2.5 ± 0.5	1.2	3.6 from 18, outside IRAC area
18	14 16 25.79	52 27 17.3		3.9 ± 0.5	2.1	outside IRAC area
17 + 18 tot			1.28	6.5 ± 1.5		
26	14 17 32.84	52 38 15.0	1.15	12 ± 2	10.1 from 27	
27	14 17 32.70	52 38 25.0	1.15	5.1 ± 1.5		multiple spots
39	14 21 19.29	53 03 22.6	1.13	14.6 ± 0.15		12.3 from 40
40	14 21 18.24	53 03 30.4	1.10	16.2 ± 0.18	1.0 0.6	
42	14 21 26.99	53 10 47.0	1.16	0.64 ± 0.09		7.5 from 43
43	14 21 26.19	53 10 49.1	1.15	2.0 ± 0.2	1.5 1.1	
50	14 22 51.01	53 36 13.9		4.4 ± 0.3		classical double morphology,
51	14 22 51.00	53 36 19.0		6.0 ± 0.4		5.5 separation
50 + 51 tot			1.27	12 ± 2		

Note. — “PB corr” is the primary beam correction, which has been applied to the flux densities in column 5. Sizes of major and minor axes are given in arcsec after deconvolving the synthesized beam. Sources are considered possible multiples if there are two resolved components within 15''. Combined flux densities are given only if the two components are potentially blended in the radio data. Systematic position uncertainties are 0.1 rms.

Table 2. Comparison with FWKK sources

FWKK name 15V	this paper name EGS06	S_5 (FWKK) (mJy)	S_5 (this paper) ^a (mJy)
02	—	0.45 ± 0.02	(0.23)
03	—	0.23 ± 0.03	<0.2
10	21	1.91 ± 0.07^b	1.0 ± 0.2
21	—	0.30 ± 0.02	(0.23)
34	19	1.31 ± 0.03	1.3
50	14	0.70 ± 0.01	0.6
70	23	0.58 ± 0.02	1.0
78	—	0.22 ± 0.04	<0.3

^aFlux densities in parentheses are below the detection threshold of this paper but were measured from the mosaics. Uncertainties in peak flux density are about 0.06 mJy/beam, and all sources are nearly pointlike at our resolution (according to FWKK) *except* 15V 10. Upper limits given are 3σ assuming point sources.

^bFWKK give the total flux density of this extended source: core and two lobes. (See FWKK Fig. 3a.) The lobes are resolved out in our BnA data, and our flux density includes only the core. Table 4 of FWKK suggests that the core comprises about 40% of the total flux density.

Table 3. IRAC Counterparts to Radio Sources

EGS06	R.A	Dec	sep('')	comments
Isolated radio sources				
1	14:15:03.89	+52:01:06.7	0.3	
2	14:14:33.33	+52:02:52.9	0.3	interacting component; see Fig. 2
3	14:14:36.76	+52:05:03.1	0.1	$z = 0.655$, old (wk [O II])
4	14:15:08.84	+52:06:42.0	0.2	
7	14:16:15.07	+52:11:21.6	0.0	
8	14:16:11.84	+52:12:04.0	0.8	
13	14:16:21.86	+52:25:03.5	0.3	
16	14:16:27.89	+52:27:07.2	0.6	X-ray
14	14:17:59.30	+52:25:53.8	0.2	edge of IRAC coverage, poor data
19	14:17:49.21	+52:28:03.2	0.1	$z = 0.996^a$, old (wk [O II]), X-ray
21	14:17:32.62	+52:32:03.3	0.2	$z = 0.986$, post-SB, X-ray
22	14:17:13.63	+52:32:13.9	0.4	$z = 0.835$, old
23	14:18:09.96	+52:33:00.4	0.2	
24	14:17:53.40	+52:35:39.6	0.3	$z = 0.679$, old
28	14:18:05.56	+52:40:32.8	0.5	$z = 1.413$, broad-line AGN
29	14:19:45.50	+52:46:48.0	0.1	
30	14:19:10.43	+52:48:30.6	0.3	$z = 0.346$, old
31	14:18:37.77	+52:51:28.6	0.4	
33	14:19:46.08	+52:56:47.1	0.8	
34	14:20:50.37	+52:57:46.9	0.3	
36	14:20:33.37	+52:58:00.9	0.1	$z = 0.570$, old
37	14:20:33.27	+53:00:03.7	0.1	
41	14:20:33.34	+53:08:21.0	0.1	
44	14:20:56.84	+53:13:07.7	0.2	$z = 0.742$, post-SB
45	14:21:54.80	+53:15:00.6	0.2	
46	14:21:27.87	+53:15:16.1	0.3	close double in R
47	14:21:37.14	+53:20:55.1	0.1	
49	14:23:12.67	+53:27:56.9	0.4	multiple in R

Table 3—Continued

EGS06	R.A	Dec	sep('')	comments
Possible radio doubles				
6	14:14:53.34	+52:10:28.8	0.2	poor data at 3.6 & 5.8 μ m
10/11	14:16:22.76	+52:19:16.4		$z = 1.600$, broad-line AGN, X-ray
26/27	14:17:32.55	+52:38:18.1		4''.1 NE of 26
39/40	14:21:18.42	+53:03:29.0		2''.1 SE of 40, $z = 0.973$, post-SB + narrow-line AGN
42/43	14:21:26.48	+53:10:48.7		2''.6 W of 43
50/51	14:22:51.02	+53:36:16.8		exposure time 0.1×normal

^aHammer et al. (1995) found $z = 0.838$ and elliptical classification for EGS06 19 = 15V 34, but the DEEP2 redshift seems secure. See Appendix A.

Note. — Redshifts and spectral classifications are from the DEEP2 survey (Davis et al. 2003). Comment “X-ray” indicates detection by either Chandra (Nandra et al. 2005) or XMM-Newton (Waskett et al. 2003).

Table 4. Photometry^a

EGS06	<i>B</i>	<i>R</i>	<i>I</i>	3.6 μ m	4.5 μ m	5.8 μ m	8.0 μ m	24 μ m
1	15.1	15.9	12.2	9.9	...
2	85.8	68.0	94.4	176.2	b
3	1.15	9.23	23.18	120.4	79.9	70.5	50.4	54
4	0.52	2.33	4.98	79.7	85.1	99.0	156.6	166
7	0.94	13.44	39.45	165.8	100.4	81.7	45.2	...
8	0.25	0.31	0.89	27.1	28.3	19.5	14.9	...
13	0.28	0.53	2.21	63.8	64.6	44.7	31.9	...
16	1.47	10.73	40.59	132.1	95.1	80.8	80.8	278
14	0.57	1.68	5.04	79.4:	78.3:	92.5:	45.4:	...
19	<0.3	2.13	7.88	111.9	80.9	57.3	40.7	...
21	0.29	2.67	8.11	78.3	57.5	41.5	36.2	...
22	0.51	7.32	26.25	164.9	106.3	76.8	48.8	...
23	17.7	20.5	21.5	28.0	22
24	0.70	10.10	29.65	149.4	88.4	70.3	40.1	...
28	1.61	3.02	4.51	42.2	49.4	52.8	65.8	77
29	9.55	21.64	28.95	123.4	148.0	198.6	359.1	598
30	10.34	90.12	171.40	268.9	211.1	130.9	85.7	...
31	37.7	42.6	26.5	10.2:	...
33	25.9	30.4	31.2	23.8	29
34	39.6	54.1	70.3	108.	139
36	2.15	25.89	59.27	175.4	116.9	88.2	47.51	...
37	18.8	23.8	24.8	21.3	225
41	3.24	30.39	102.40	249.6	149.7	126.1	77.3	...
44	24.39	48.98	100.00	418.0	252.1	189.7	150.2	27
45	0.19	0.35	2.28	106.4	100.6	71.8	61.5	25
46	0.37	3.06	12.85	134.0	96.0	61.8	43.3	...
47	0.69	1.70	3.70	96.0	100.1	71.4	53.0	...
49	31.1	36.5	30.4	31.2	57
6	...	46.13	101.8:	388.0	293.2	232.9	125.1	...
10/11	1.46	5.73	14.43	185.4	267.9	365.4	561.8	792

Table 4—Continued

EGS06	<i>B</i>	<i>R</i>	<i>I</i>	3.6 μ m	4.5 μ m	5.8 μ m	8.0 μ m	24 μ m
26/27	1.90	19.12	53.26	223.0	154.7	138.4	126.1	109
39/40	3.34	9.38	29.03	142.8	109.2	86.7	115.8	894
42/43	99.7	92.9	61.4	43.9	...
50/51	7.17	60.87	112.20	177.2	142.6	...	60.2	...
noise ^c	0.08	0.10	0.19	0.2	0.2	1.2	1.2	18

^aFlux densities in μ Jy. Colon indicates photometric uncertainty $\gtrsim 30\%$.

^bBlended with other sources; see Fig. 2.

^cTypical uncertainty from photon noise alone. See text for discussion of additional measurement uncertainties.